

Bayesian inference of neural connectivity in a population of neurons from calcium imaging data

us

(Dated: August 7, 2009)

We present Bayesian framework for inferring connectivity in a network of coupled neurons, observed simultaneously using calcium imaging.

Contents

I. Introduction	1
II. Methods	2
A. Model	2
B. Goal and general strategy	4
C. Initialization of “internal” parameters via sequential Monte Carlo methods	4
D. Estimating joint posteriors over weakly coupled neurons	5
1. A cheaper high-SNR approximation of the joint posteriors	6
E. Estimating the functional connectivity matrix	6
1. Imposing a sparse prior on the functional connectivity	7
2. Imposing Dale’s law on the functional connectivity	7
F. Specific implementation notes	7
III. Results	7
A. Simulating neural activity in a neural population	7
B. Inferring functional connectivity from the simulated calcium imaging data	8
C. Scale bias in inferred connection weights due to coarse time discretization of calcium imaging data	9
D. Impact of different imaging frame rates, durations, and noise levels on the inference	11
E. Accuracy of the estimates and Fisher information matrix	12
F. Impact of using priors on the inference	14
G. Impact of strong correlations and deviations from generative model on the inference	14
IV. Discussion	15
Acknowledgements	17
References	17

I. INTRODUCTION

Since Ramon y Cajal discovered that the brain is a rich and dense *network* of neurons, neuroscientists have wondered about the details of these networks. Since then, while much has been learned about “macro-circuits” — the connectivity between populations of neurons — relatively little is known about “micro-circuits” — the connectivity within populations of neurons. Broadly, one can imagine two distinct strategies for inferring microcircuit connectivity: anatomical and functional. Anatomical approaches to inferring circuitry include any strategy that does not consider the neural *activity*. Recently developed technologies including array tomography [30], brainbow mice [28], and serial electron microscopy based approaches [7], are rapidly improving and show great promise. This work takes a functional approach, i.e., our aim is to be able to infer the microcircuit by only observing the activity of a population of neurons.

Experimental tools that enable approximately simultaneous observations of the activity many (e.g., $O(10^3)$) neurons are now widely available. While arrays of extracellular electrodes have been exploited for this purpose, those used in vivo are inadequate for inferring monosynaptic connectivity, as the inter-electrode spacing is typically too large (however, multi-electrode arrays in slice and retina do not share this problem, see for example [41]). Alternately, calcium-sensitive fluorescent indicators provide a glimpse into the spiking activity of many neighboring neurons [59], which are more likely to be connected [1, 6]. Some organic dyes achieve signal-to-noise ratios (SNRs) yielding

single spike resolution [64]. In combination with these dyes, bulk-loading techniques enable experimentalists to simultaneously fill populations of neurons with such dyes [54]. In addition, genetically encoded calcium indicators are under rapid development from a number of groups, and are approaching SNR levels of nearly single spike accuracy as well [62]. Microscopy technologies for collecting fluorescence signals are also rapidly developing. Cooled CCDs for wide-field imaging (either epifluorescence or confocal) now achieve a quantum efficiency of $\approx 90\%$ with frame rates easily exceeding 30 or 60 Hz [14]. For in vivo work, 2-photon laser scanning microscopy can achieve similar frame rates, by designing software to efficiently control the typical scanners (Valentin Naegerl, Tom Mrsic-Flogel, and Bruno Pichler, personal communications), using acoustic-optical deflectors to focus light at arbitrary locations in (three-dimensional) space [24, 44, 45, 48], or using resonant scanners [36]. Together, these experimental tools can provide movies indicating calcium based fluorescent transients for small populations of neurons (e.g., $O(10^2)$), with “reasonable” SNR, at 30 Hz, both in the in vitro and in vivo scenarios.

Given these experimental advances in functional neural imaging, we aim here to develop complementary computational tools. We first define a coupled hidden Markov Model, relating the observed variables (fluorescence traces from observable neurons) to the hidden variables (spike trains of those neurons), as governed by a small set of parameters, including the functional connectivity matrix. Given this model, we derive an expectation maximization (EM) algorithm, to approximate the maximum a posteriori estimates of the parameters of interest. Because our model is high dimensional, non-linear, and non-Gaussian, the E step must be approximated. Standard sampling procedures, such as sequential monte carlo, are known to perform poorly in such scenarios [?]. We therefore develop a novel embedded-chain-within-blockwise-Gibbs approach to overcome these obstacles [33]. This strategy enables us to accurately infer the functional connection matrix from a small (e.g., ≈ 200) population of neurons, making realistic assumptions about dynamics and observation parameters. By introducing a factorization approximation, we still perform nearly as well, and greatly reduce the computational burden. Furthermore, imposing biophysically based priors leads to a comparable reduction in the amount of data required to obtain satisfactory estimates. We then quantify the accuracy of our estimates as a function of imaging rate, noise, experimental duration, number of neurons, strong spiking correlations, and certain model misspecifications. Given realistic assumptions about the dynamics and noise parameters, we show that 10 minutes of data imaged at 30 Hz from 200 neurons requires is sufficient for us to accurately estimate the functional connection matrix of the observable neurons, and only requires about 10 minutes of processing on a cluster.

II. METHODS

A. Model

We first describe a parametric generative model that characterizes the statistics of the (unobserved) joint spike trains of all N observable neurons, along with the observed calcium fluorescence data. Each neuron is modeled as a generalized linear model (GLM); this class of model is known to capture the statistical firing properties of the of individual neurons fairly accurately [8, 9, 12, 25, 37–39, 41, 42, 47, 53, 58, 60]. We denote the i -th neuron’s activity at time t as $n_i(t)$: in continuous time, $n_i(t)$ could be modeled as an unmarked point process, but we will take a discrete-time approach here, and so $n_i(t)$ will be a binary random variable. We model the spiking probability of neuron i via an instantaneous nonlinear function, $f(\cdot)$, of the filtered and summed input to that neuron at that time, $J_i(t)$. The input is composed of: (i) some baseline value, b_i ; (ii) some external stimulus, $S(t)$, that is linearly filtered by k_i ; and (iii) spike history terms, $h_j(t)$, from each neuron j , weighted by w_{ij} :

$$n_i(t) \stackrel{iid}{\sim} \text{Bernoulli}(f(J_i(t))), \quad J_i(t) = b_i + k_i \cdot S(t) + \sum_{j=1}^N w_{ij} h_j(t). \quad (1)$$

To ensure computational tractability, we must impose some reasonable constraints on the instantaneous nonlinearity $f(\cdot)$ (which plays the role of the inverse of the link function in the standard GLM setting) and on the dynamics of the spike-history effects $h_j(t)$. More specifically, first, we restrict our attention to functions $f(\cdot)$ which ensure the concavity of the spiking loglikelihood in this model [38], as we will discuss at more length below. In this paper, we use

$$f(J) = P[X > 0 | X \sim \text{Poiss}(e^J \Delta)] = 1 - \exp[-e^J \Delta] \quad (2)$$

(where the inclusion of Δ , the time step size, ensures that the firing rate scales properly with respect to the time discretization), though in our experience the results depend only weakly on the details of $f(\cdot)$ within the class of log-concave models [27, 38]; see [18] for a proof that this $f(\cdot)$ satisfies the required concavity constraints.

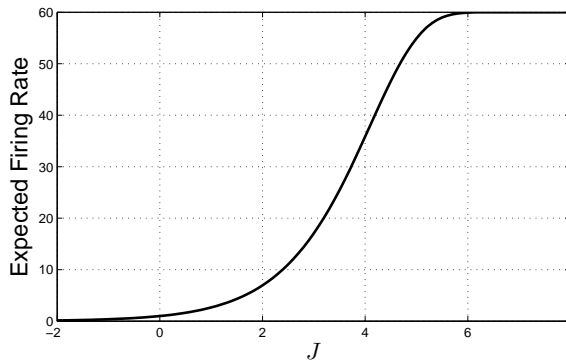


FIG. 1: Given our model, Eq. 1, the relationship between firing rate and the magnitude of the input to a neuron is highly nonlinear. Note that firing rate saturates at $1/\Delta$, because of our Bernoulli assumption.

Second, because the algorithms we develop below assume Markovian dynamics, we model the spike history terms as:

$$h_j(t) = (1 - \Delta/\tau_h)h_j(t - \Delta) + n_j(t) + \sigma_h\sqrt{\Delta}\epsilon_j^h(t), \quad (3)$$

where τ_h is the decay time constant for spike history terms, σ_h is a standard deviation parameter, $\sqrt{\Delta}$ ensures that the statistics of this Markov process have a proper Ornstein-Uhlenbeck limit as $\Delta \rightarrow 0$, and throughout this paper, ϵ denotes an independent standard normal random variable. Note that this model generalizes (via a simple augmentation of the state variable $h_j(t)$) to allow each neuron to have several spike history terms, each with a unique time constant, which when weighted and summed allow us to model a wide variety of possible post-synaptic effects, including bursting, facilitating, and depressing synapses; see [61] for further details. In this paper, for simplicity, we assume that τ_h and σ_h are known synaptic parameters, and therefore our model spiking parameters θ^n are given by $\{\theta_i^n\}_{i=1}^N$, where $\theta_i^n = \{\mathbf{w}_i, k_i, b_i\}$, with $\mathbf{w}_i = (w_{i1}, \dots, w_{iN})$.

The problem of estimating the connectivity parameters \mathbf{w}_i in this type of GLM, given a fully-observed ensemble of neural spike train $\{n_i(t)\}$, has recently received a great deal of attention; see the references above for a partial list. In the calcium fluorescent imaging setting, however, we do not directly observe spike trains; $\{n_i(t)\}$ must be considered a hidden variable here. Instead, each spike in a given neuron leads to a rapid increase in the intracellular calcium concentration, which then decays slowly due to various cellular buffering and extrusion mechanisms. We in turn make only noisy, indirect, and subsampled observations of this intracellular calcium concentration, via fluorescent imaging techniques [64]. To perform statistical inference in this setting, [61] proposed a simple conditional first-order hidden Markov model (HMM) for the intracellular calcium concentration $C_i(t)$ in cell i at time t , along with the observed fluorescence $F_i(t)$:

$$C_i(t) = C_i(t - \Delta) + (C_i^b - C_i(t - \Delta))\Delta/\tau_i^c + A_i n_i(t) + \sigma_i^c \sqrt{\Delta} \epsilon_i^c(t), \quad (4)$$

$$F_i(t) = \alpha_i S(C_i(t)) + \beta_i + \sqrt{\gamma_i S(C_i(t)) + \sigma_i^F} \epsilon_i^F(t). \quad (5)$$

This model can be interpreted as a simple driven autoregressive process: under nonspiking conditions, $C_i(t)$ fluctuates around the baseline level of C_i^b , driven by normally-distributed noise $\epsilon_i^c(t)$ with standard deviation $\sigma_i^c \sqrt{\Delta}$. Whenever the neuron fires a spike, $n_i(t) = 1$, causing the calcium variable $C_i(t)$ to jump by a fixed amount A_i , and subsequently decay with time constant τ_i^c . The fluorescence signal $F_i(t)$ corresponds to the count of photons collected at the detector per neuron per imaging frame. This photon count may be modeled with normal statistics, with the mean and variance given by generalized Hill functions, where $S(C) = C/(C + K_d)$ [63]. Because the parameter K_d effectively acts as a simple scale factor, and is a property of the fluorescent indicator, we assume throughout this work that it is known.

To summarize, Eqs. 1 – 5 define a coupled HMM: the underlying spike trains $n_i(t)$ and spike history terms $h_i(t)$ evolve in a Markovian manner, driving the intracellular calcium concentrations $C_i(t)$, which are themselves Markovian, but evolving at a slower timescale τ_i^c . Finally, we observe only the fluorescence signals $\{F_i(t)\}$, which are related in a simple Markovian fashion to the calcium variables $C_i(t)$.

B. Goal and general strategy

Our primary goal is to estimate the connectivity matrix, \mathbf{w} , given the observed set of calcium fluorescence signals \mathbf{F} . We must also deal with a number of nuisance parameters: the spiking parameters $\{k_i, b_i\}$ and the calcium parameters $\{C_i^b, \tau_i^c, A_i, \sigma_i^c, \alpha_i, \beta_i, \gamma_i, \sigma_i^F\}$. We addressed the problem of estimating these latter parameters in earlier work [61]; thus our focus here will be on \mathbf{w} . A Bayesian approach is natural here, since we have a good deal of prior information about neural connectivity; see [47] for a related discussion. However, a fully-Bayesian approach, in which we numerically integrate over the very high-dimensional parameter $\theta = \{\mathbf{w}, k_i, b_i, C_i^b, \tau_i^c, A_i, \sigma_i^c, \alpha_i, \beta_i, \gamma_i, \sigma_i^F\}$, is not particularly attractive here, from a computational point of view. Thus we take a compromise approach and compute *maximum a posteriori* (MAP) estimates for the parameters via an expectation-maximization (EM) algorithm in which the sufficient statistics are computed by a hybrid blockwise Gibbs sampler and sequential Monte Carlo (SMC) method.

More specifically, we iterate the steps:

E step: Evaluate $Q(\theta^{(l+1)}, \theta^{(l)}) = E_{P[\mathbf{X}|\mathbf{F}, \theta^{(l+1)}]} \ln P[\mathbf{F}, \mathbf{X}|\theta^{(l)}] = \int P[\mathbf{X}|\mathbf{F}; \theta^{(l+1)}] \ln P[\mathbf{F}, \mathbf{X}|\theta^{(l)}] d\mathbf{X}$

M step: Solve $\theta^{(l+1)} = \underset{\theta}{\operatorname{argmax}} \left\{ Q(\theta, \theta^{(l)}) + \ln P(\theta) \right\}$,

where \mathbf{X} denotes the set of all hidden variables $\{C_i(t), n_i(t), h_i(t)\}_{i \leq N, t \leq T}$ and $P(\theta)$ denotes a (possibly improper) prior on the parameter space θ . According to standard EM theory [13, 29], each iteration of these two steps is guaranteed to increase the log-posterior $\ln P(\theta^{(l+1)}|\mathbf{F})$, and will therefore lead to at least a locally maximum a posteriori estimator.

Now our major challenge is to evaluate the auxiliary function $Q(\theta^{(l+1)}, \theta^{(l)})$ in the E-step. Because our model is a coupled HMM, as discussed in the previous section, Q simplifies considerably [43]:

$$\begin{aligned} Q(\theta, \theta^{(l)}) &= \sum_{it} P[C_i(t)|\mathbf{F}; \theta] \times \ln P[F_i(t)|C_i(t); \alpha_i, \beta_i, \gamma_i, \sigma_i^F] \\ &+ \sum_{it} P[C_i(t), C_i(t - \Delta), n_i(t)|\mathbf{F}; \theta] \times \ln P[C_i(t)|C_i(t - \Delta), n_i(t); C_i^b, \tau_i^c, A_i, \sigma_i^c] \\ &+ \sum_{it} P[n_i(t), \mathbf{h}(t)|\mathbf{F}; \theta] \times \ln P[n_i(t)|\mathbf{h}(t); b_i, k_i, \mathbf{w}_i, S(t)], \end{aligned} \quad (6)$$

where $\mathbf{h}(t) = \{h_i(t)\}_{i=1}^N$. Thus we need only compute low-dimensional marginals of the full posterior distribution $P[\mathbf{X}(t)|\mathbf{F}; \theta]$; specifically, we need pairwise marginals, of the form $P[X_i(t), X_i(t - 1)|\mathbf{F}; \theta]$. The high dimensionality of the hidden variable \mathbf{X} necessitates the development of specialized blockwise Gibbs-SMC sampling methods, as we describe in sections II C and II D below. Once we have obtained these marginals, the M-step breaks up into a number of independent optimizations that may be computed in parallel and which are therefore relatively straightforward (section II E); see section II F for a pseudocode summary along with some specific implementation details.

C. Initialization of “internal” parameters via sequential Monte Carlo methods

We begin by constructing relatively cheap, approximate preliminary estimators for the nuisance parameters $\theta \setminus \mathbf{w}_{ij}$, i.e., the observation parameters, $\{\alpha_i, \beta_i, \gamma_i, \sigma_i^F\}$, the calcium dynamics parameters $\{C_i^b, \tau_i^c, A_i, \sigma_i^c\}$, and the intrinsic dynamics parameters, $\{b_i, w_{ii}\}$ (note that we include all the parameters except w_{ij} for $i \neq j$). The idea is to initialize our estimate $\theta^{(0)}$ by assuming that each neuron is observed independently. Thus we want to compute $P[X_i(t), X_i(t - \Delta)|\mathbf{F}_i; \theta_i]$, and solve the M-step for each individual parameter θ_i , with the connection matrix \mathbf{w} held fixed. This single-neuron case is much simpler, and has been discussed at length in [61]; therefore, we only provide a brief overview here. The standard forward and backward recursions provide these posteriors [50]:

$$P[X_i(t)|F_i(0:t)] \propto P[F_i(t)|X_i(t)] \int P[X_i(t)|X_i(t - \Delta)] P[X_i(t - \Delta)|F_i(0:t - \Delta)] dX_i(t - \Delta) \quad (7)$$

$$P[X_i(t), X_i(t - \Delta)|F_i] = P[X_i(t)|F_i] \frac{P[X_i(t)|X_i(t - \Delta)] P[X_i(t - \Delta)|F_i(0:t - \Delta)]}{\int P[X_i(t)|X_i(t - \Delta)] P[X_i(t - \Delta)|F_i(0:t - \Delta)] dX_i(t - \Delta)}, \quad (8)$$

where we have dropped the conditioning on the parameters θ for brevity’s sake. Because these integrals cannot be analytically evaluated for our model, we approximate them using SMC (“marginal particle filtering”) methods

[16, 17, 21]; see [61] for details on the proposal density and resampling methods used here. The output of these SMC techniques comprise an array of particle positions $\{X_i^{(l)}(t)\}$, where l indexes the particle number, and a discrete approximation to the marginals $P[X_i(t), X_i(t - \Delta)|F_i]$,

$$P[X_i(t), X_i(t - \Delta)|F_i] \approx \sum_{j,l} r_i^{(j,l)}(t, t - \Delta) \delta[X_i(t) - X_i^{(l)}(t)] \times \delta[X_i(t - \Delta) - X_i^{(j)}(t - \Delta)], \quad (9)$$

where $r_i^{(j,l)}(t, t - \Delta)$ denotes the weight attached to the particle pair with positions $(X_i^{(l)}(t), X_i^{(j)}(t - \Delta))$.

As discussed above, the sufficient statistics for estimating the parameters for each neuron, θ_i , are exactly these marginal posteriors. As shown in Eq. 6, the M-step decouples into three independent subproblems. The first term depends on only $\{\alpha_i, \beta_i, \gamma_i, \sigma_i\}$; since $\ln P[F_i(t)|C_i(t); \theta_i]$ is quadratic (by our Gaussian assumption on the fluorescent observation noise), we can estimate these parameters by solving a weighted regression problem (specifically, we use a coordinate-optimization approach: we solve a quadratic problem for $\{\alpha_i, \beta_i\}$ while holding $\{\gamma_i, \sigma_i\}$ fixed, then estimate $\{\gamma_i, \sigma_i\}$ by the usual residual error formulas while holding $\{\alpha_i, \beta_i\}$ fixed). Similarly, the second term requires us to optimize over $\{\tau_i^c, A_i, C_i^b\}$ using a quadratic solver, and then we use the residuals to estimate σ_i^c . Note that all the parameters mentioned so far are constrained to be non-negative, but may be solved efficiently using standard quadratic program solvers. Finally, the last term, assuming neurons are independent, may be expanded:

$$E[\ln P[n_i(t), \mathbf{h}_i(t)|\mathbf{F}; \theta]] = P[n_i(t), h_i(t)|F_i] \ln f(J_i(t)) + (1 - P[n_i(t), h_i(t)|F_i]) \ln[1 - f(J_i(t))]; \quad (10)$$

since $J_i(t)$ is a linear function of (b_i, k_i, \mathbf{w}_i) , and the right-hand side of (10) is concave in $J_i(t)$, we see that the third term in 6 is a sum of terms which are concave in (b_i, k_i, \mathbf{w}_i) , and may therefore be solved efficiently using any convex optimization method, e.g. Newton-Raphson or conjugate gradient ascent.

Our procedure therefore is to initialize the parameters for each neuron using some default values that we have found to be effective in practice, and then recursively (i) estimate the marginal posteriors (E step), and (ii) maximize the parameters (M step), using the above described approach. We iterate these two steps until the change in parameters does not exceed some minimum threshold. We can then use the marginal posteriors from the last iteration to seed the blockwise Gibbs sampling procedure described below, to obtain a rough estimate of $P[\mathbf{h}(t)|\mathbf{F}]$.

D. Estimating joint posteriors over weakly coupled neurons

Now we turn to the key problem: computing $P(\mathbf{h}(t), n_i(t)|F, \theta)$, which encapsulates the sufficient statistics for estimating the connectivity matrix \mathbf{w} (recall equation (6)). The SMC methods described in the preceding section only provide the marginals over each neuron, $P[X_i(t)|F_i; \theta_i]$; these methods may in principle be extended to obtain the desired full posterior $P[\mathbf{X}(t)|\mathbf{F}; \theta]$, but since the SMC algorithm is fundamentally a sequential importance sampling method, these techniques scale poorly as the dimensionality of the hidden state $\mathbf{X}(t)$ increases [3]. Thus we need a different approach.

One very simple idea is to use a Gibbs sampler: sample sequentially from

$$X_i(t) \sim P[X_i(t)|\mathbf{X}_{\setminus i}, X_i(0), \dots, X_i(t - \Delta), X_i(t + \Delta), \dots, X_i(T), \mathbf{F}; \theta], \quad (11)$$

looping in some order over all cells i and all time bins t . Unfortunately, this approach is likely to mix very poorly, due to the strong temporal dependence between $X_i(t)$ and $X_i(t + \Delta)$. Instead, we propose to use a blockwise Gibbs strategy, sampling each spike train as a block:

$$X_i \sim P[X_i|\mathbf{X}_{\setminus i}, \mathbf{F}; \theta]; \quad (12)$$

if we can draw these blockwise samples $X_i = \{X_i(t)\}$ efficiently for a large subset of timebins t simultaneously, then we would expect the resulting Markov chain to mix much more quickly than the naive element-wise Gibbs chain, since by assumption the hidden variables X_i, X_j are weakly dependent for different cells $i \neq j$, and Gibbs is most efficient for weakly-dependent variables.

So, how can we efficiently sample from $P[X_i|\mathbf{X}_{\setminus i}, \mathbf{F}; \theta]$? One attractive approach is to try to repurpose the SMC methods described above, which are quite effective for drawing approximate samples from $P[X_i|\mathbf{X}_{\setminus i}, \mathbf{F}; \theta]$ for one neuron i at a time. Recall that sampling from an HMM is in principle easy by the “propagate forward, sample backward” method: we first compute the forward probabilities $P[X_i(t)|\mathbf{X}_{\setminus i}(0:t), \mathbf{F}(0:t); \theta]$ recursively for timesteps

0 up to T , then sample backwards from $P[X_i(t)|\mathbf{X}_{\setminus i}(0:T), \mathbf{F}(0:T), X_i(t+\Delta); \theta]$. This approach is powerful because each sample requires just linear time to compute (i.e., $O(T/\Delta)$ time, where T/Δ is the number of desired time steps). Unfortunately, in this case we can only compute the forward probabilities approximately (with the SMC forward recursion (7)), and so therefore this attractive forward-backward approach only provides approximate samples from $P[X_i|\mathbf{X}_{\setminus i}, \mathbf{F}; \theta]$, not the exact samples required to establish the validity of the Gibbs method.

Of course, in principle we should be able to use the Metropolis-Hastings (M-H) algorithm to correct these approximate samples. The problem is that the M-H acceptance ratio in this setting involves a high-dimensional integral over the set of paths that the particle filter might possibly trace out, and is therefore difficult to compute directly. [2] discuss this problem at more length, along with some proposed solutions. However, a slightly simpler approach was introduced by [34]. Their idea is to exploit the $O(T/\Delta)$ forward-backward sampling method by embedding a discrete Markov chain within the continuous state space \mathcal{X}_t ; the state space of this discrete embedded chain is sampled randomly according to some distribution ρ_t with support on \mathcal{X}_t . It turns out that an appropriate acceptance probability (defined in terms of the original state space model transition and observation probabilities, along with the auxiliary sampling distributions ρ_t) may be computed quite tractably, guaranteeing that the samples produced by this algorithm form a Markov chain with the desired equilibrium density. See [34] for details.

We can apply this embedded-chain method quite directly here to sample from $P[X_i|\mathbf{X}_{\setminus i}, \mathbf{F}; \theta]$. The one remaining question is how to choose the auxiliary densities ρ_t . We would like to choose these densities to be close to the desired marginal densities $P[X_i(t)|\mathbf{X}_{\setminus i}, \mathbf{F}; \theta]$, and conveniently, we have already computed a good (discrete) approximation to these densities, using the SMC methods described in the last section. The algorithm described in [34] requires that ρ_t be continuous densities, so we simply convolve our discrete SMC-based approximation (specifically, the marginal of (9)) with an appropriate normal density to arrive at a very tractable mixture-of-Gaussians representation for ρ_t .

Thus, to summarize, our procedure for sampling from the desired joint state distributions $P(\mathbf{h}(t), n_i(t)|F, \theta)$ has a Metropolis-within-blockwise-Gibbs flavor, where the internal Metropolis step is replaced by the $O(T/\Delta)$ embedded-chain method introduced by [34], and the auxiliary densities ρ_t necessary for implementing the embedded-chain sampler are obtained using the SMC methods from [61].

1. A cheaper high-SNR approximation of the joint posteriors

If the SNR in the calcium imaging is sufficiently high, then by definition the observed fluorescence data F_i will provide enough information to exactly determine the underlying hidden variables X_i . Thus, in this case the joint posterior approximately factorizes into a product of marginals for each neuron i :

$$P[\mathbf{X}|\mathbf{F}; \theta] \approx \prod_{i=1}^N P[X_i|F_i; \theta]. \quad (13)$$

We can take advantage of this representation because we have already estimated all the above marginals using the SMC methods described in section II C. In particular, we can obtain the sufficient statistics $P(\mathbf{h}(t), n_i(t)|\mathbf{F}, \theta)$ by forming a product over the marginals $P(X_i(t)|\mathbf{F}_i, \theta)$ obtained from (9). This approximation entails a very significant gain in efficiency for two reasons: first, it obviates the need to generate joint samples via the expensive blockwise-Gibbs approach described above; and second, because we can very easily parallelize the SMC step, inferring the marginals $P[X_i(t)|\mathbf{F}_i; \theta_i]$ and estimating parameters θ_i for each neuron on a separate processor. We will discuss the empirical accuracy of this approximation in more depth in the Results section.

E. Estimating the connectivity matrix

Computing the M-step for the connectivity matrix, \mathbf{w} , is an optimization problem with on the order of N^2 variables. By construction, however, the auxiliary function (6) is concave in \mathbf{w} , and decomposes into N terms which may be optimized independently using standard ascent methods. To improve our estimates, we will incorporate two sources of strong *a priori* information via our prior $P(\mathbf{w})$: first, prior anatomical studies have established that connectivity in many neuroanatomical substrates is “sparse,” i.e., most neurons form synapses with only a fraction of their neighbors [4, 10, 19, 20, 23, 32, 40, 46, 51, 55], implying that many elements of the connectivity matrix \mathbf{w} are zero; see also [38, 41, 47, 52] for further discussion. Second, “Dale’s law” states that each of a neuron’s postsynaptic connections in adult cortex (and many other brain areas) must all be of the same sign (either excitatory or inhibitory). Both of these priors are easy to incorporate in the M-step optimization, as we discuss below.

1. Imposing a sparse prior on the functional connectivity

Enforcing sparseness for signal recovered with a series of linear measurements via $L1$ -regularizer is known to dramatically reduce the amount of data necessary to accurately reconstruct the signal [11, 15, 31, 35, 56, 57]. We incorporate a prior of the form $\ln p(\mathbf{w}) = \text{const.} - \lambda \sum_{i,j} |w_{ij}|$, and additionally enforce the constraints $|w_{ij}| < m$, for a suitable constant m (since both excitatory and inhibitory cortical connections are known to be bounded in size). Since the penalty $\ln p(\mathbf{w})$ is concave, and the constraints $|w_{ij}| < m$ are convex, we may still solve the resulting optimization problem in the M-step using standard convex optimization methods [5]. In addition, the problem retains its separable structure: the full optimization may be broken up into N smaller problems that may be solved independently.

2. Imposing Dale's law on the functional connectivity

Enforcing Dale's law requires us to solve a non-convex, non-separable problem: we need to optimize the concave function $Q(\theta, \theta^{(l)}) + \ln P(\theta)$ under the non-convex, non-separable constraint that all of the columns of the matrix \mathbf{w} are of a fixed sign (either nonpositive or nonnegative). It is difficult to solve this problem exactly, but we have found that simple greedy methods are quite efficient in finding good (possibly approximate) solutions. We begin with our original sparse solution, obtained as discussed in the previous subsection without enforcing Dale's law. Then we assign each neuron as either excitatory or inhibitory, based on the weights we have inferred in the previous step: i.e., neurons i whose inferred postsynaptic connections w_{ij} are largely positive are tentatively labeled excitatory, and neurons with largely inhibitory inferred postsynaptic connections are labeled inhibitory. Neurons which are highly ambiguous may be unassigned in the early iterations, to avoid making mistakes from which it might be difficult to recover. Given the assignments a_i ($a_i = 1$ for putative excitatory cells, -1 for inhibitory, and 0 for neurons which have not yet been assigned) we solve the convex, separable problem

$$\underset{a_i w_{ij} \geq 0 \ \forall i,j}{\operatorname{argmax}} \quad Q(\theta, \theta^{(l)}) + \ln P(\theta), \quad (14)$$

which may be handled using the standard convex methods discussed above. Given the new estimated connectivities \mathbf{w} , we can re-assign the labels a_i , or even flip some randomly to check for local optima. We have found this simple approach to be fairly effective in practice.

F. Specific implementation notes

Pseudocode summarizing our approach is given in Algorithm 1, and the data (or simulation) processing pipeline is shown diagrammatically in Figure 2. As discussed in section II C, the “internal” parameters $\theta \backslash \mathbf{w}_{ij}$ may be initialized effectively using the methods described in [61]; then the full parameter θ is estimated via EM, where we use the embedded-chain-within-blockwise-Gibbs approach discussed in section II D (or the cheaper factorized approximation described in section II D 1) to obtain the sufficient statistics in the E step and the separable convex optimization methods discussed in section II E for the M step.

As emphasized above, the parallel nature of these EM steps is essential for making these computations tractable. We performed the bulk of our analysis on a high-performance cluster of Intel Xeon L5430 based computers (2.66 GHz). For 10 minutes of simulated fluorescence data, imaged at 30 Hz, calculations typically took 10-20 minutes per neuron using the factorized approximation, with time split approximately equally between (i) estimating the internal parameters $\theta \backslash \mathbf{w}_{ij}$, (ii) approximating the posteriors using the independent SMC method, and (iii) estimating the functional connectivity matrix, \mathbf{w} . The hybrid embedded-chain-within-blockwise-Gibbs sampler was substantially slower, up to an hour per neuron per Gibbs pass, with the Gibbs sampler dominating the computation time (because the Gibbs process requires 5 Gibbs loops, each requiring about 5 MCMC forward-backward passes).

III. RESULTS

A. Simulating neural activity in a neural population

To test the described method for inferring functional connectivity from calcium imaging data, we simulated networks (according to our model, Eqs. 1 – 5) of stochastically connected neurons. Although simulations ran at 1 msec time

Algorithm 1 Pseudocode for estimating functional connectivity from calcium imaging data using EM; η^n , η^F , N_G are user-defined convergence tolerance parameters. XXX CAN WE INDENT THE BELOW PROPERLY? WOULD MAKE IT MORE LEGIBLE. ALSO, IT IS NOT EXACTLY CORRECT NOW XXX

```

while  $\|\mathbf{w}^{(l)} - \mathbf{w}^{(l-1)}\| > \eta^w$  do
  for all  $i = 1 \dots N$  do
    while  $|\theta_i^{(l)} - \theta_i^{(l-1)}| > \eta^F$  do
      Approximate  $P[X_i(t)|F_i; \theta]$  using SMC (section II C)
      Perform the M-step for the “internal” parameters  $\theta \setminus \mathbf{w}_{ij}$  (section II C)
    end while
  end for
  for all  $i = 1 \dots N$  do
    Approximate  $P[n_i(t), \mathbf{h}(t)|\mathbf{F}; \theta]$  using either the blockwise Gibbs method or the high-SNR factorized approximation (section II D)
  end for
  for all  $i = 1 \dots N$  do
    Perform the M-step using separable convex optimization methods (section II E)
  end for
end while

```

discretization, imaging rate was assumed to be much slower. Simulations lasted anywhere between 5 minutes and 1 hours (of simulated time). Model parameters were chosen based on experimental data available from the literature [6, 22, 26, 49].

More specifically, the network was divided into excitatory (80%) and inhibitory (20%) neurons [6, 22], each respecting Dale’s law, i.e., each neurons was either excitatory or inhibitory (corresponding to all positive or all negative columns in our functional connection weight matrix, \mathbf{w}). Neurons were randomly connected to each other with probability 0.1 [6, 26]. Synaptic weights for excitatory connections, as defined by EPSP peak amplitude, were randomly drawn from exponential distribution with the mean of $0.5\mu V$ [26, 49]. To convert these into functional connectivity weights, we note that $w_{ij} = 1$ corresponds to a jump in $J_i = 1$, immediately following a spike from neuron j . Defining V_δ as the difference between threshold and rest for a neuron, and V_E as the peak amplitude of an EPSP (and similarly for IPSP’s), we can say the change in probability after a spike is $\Delta P = V_E/V_\delta$. Because Eq. 1 provides the same quantity in our model parameter, w_{ij} , we have:

$$w_{ij} = \ln(-\ln(e^{-r_i\tau_w} - V_E/V_\delta)/r_i\tau_w), \quad (15)$$

where $r_i = \exp(b_i)$ is the base firing rate of neuron i and $\tau_w = 10$ msec was the typical EPSP/IPSP scale over which single EPSP affects the firing probability of the neuron i . Inhibitory connections were also drawn from exponential distribution; their strengths chosen so as to balance excitatory and inhibitory currents in the network, and achieve an average firing rate of ≈ 5 Hz. Practically, the mean strength of inhibitory connections was about 10 times larger than that of the excitatory connections. PSP shapes were modeled as the difference of two exponentials, corresponding to a sharp rise and relatively slow decay [49]. We neglected conduction delays, given that the time delay below ~ 1 msec expected in local cortical circuit was smaller than the time step of our computer simulation. Each neuron also had an exponential refractory current with a 10 msec time constant. XXX Y: did that not get sampled from some distribution? XXX

Parameters for the calcium dynamics and observation statistics were chosen according to our experience with several cells analyzed using algorithm of [61]. Each parameter was generated from a normal distribution with specified mean and variance at about 30% of the mean, truncated at the lower bound at about 30% of the mean value. Table I provides details for each of the parameters in our model.

B. Inferring functional connectivity from the simulated calcium imaging data

With neural population activity prepared as described in the previous section, we used our inference algorithms to reconstruct the functional connectivity matrix from simulated fluorescence data. Specifically, we estimated the connectivity matrix by maximizing $E[\ln P[n_i(t)|\mathbf{h}(t); b_i, \mathbf{w}_i]]$ with respect to $\{b_i, \mathbf{w}_i\}$, for each neuron (c.f. Eq. 6), using both the embedded-chain-within-blockwise-Gibbs approach as well as using factorized approximation, Figure 4. We found that factorized approximation algorithm was able to provide reconstructions almost as accurate as the exact embedded-chain-within-blockwise-Gibbs approach — $r^2 = 0.47$ versus $r^2 = 0.48$ — when parameters corresponded

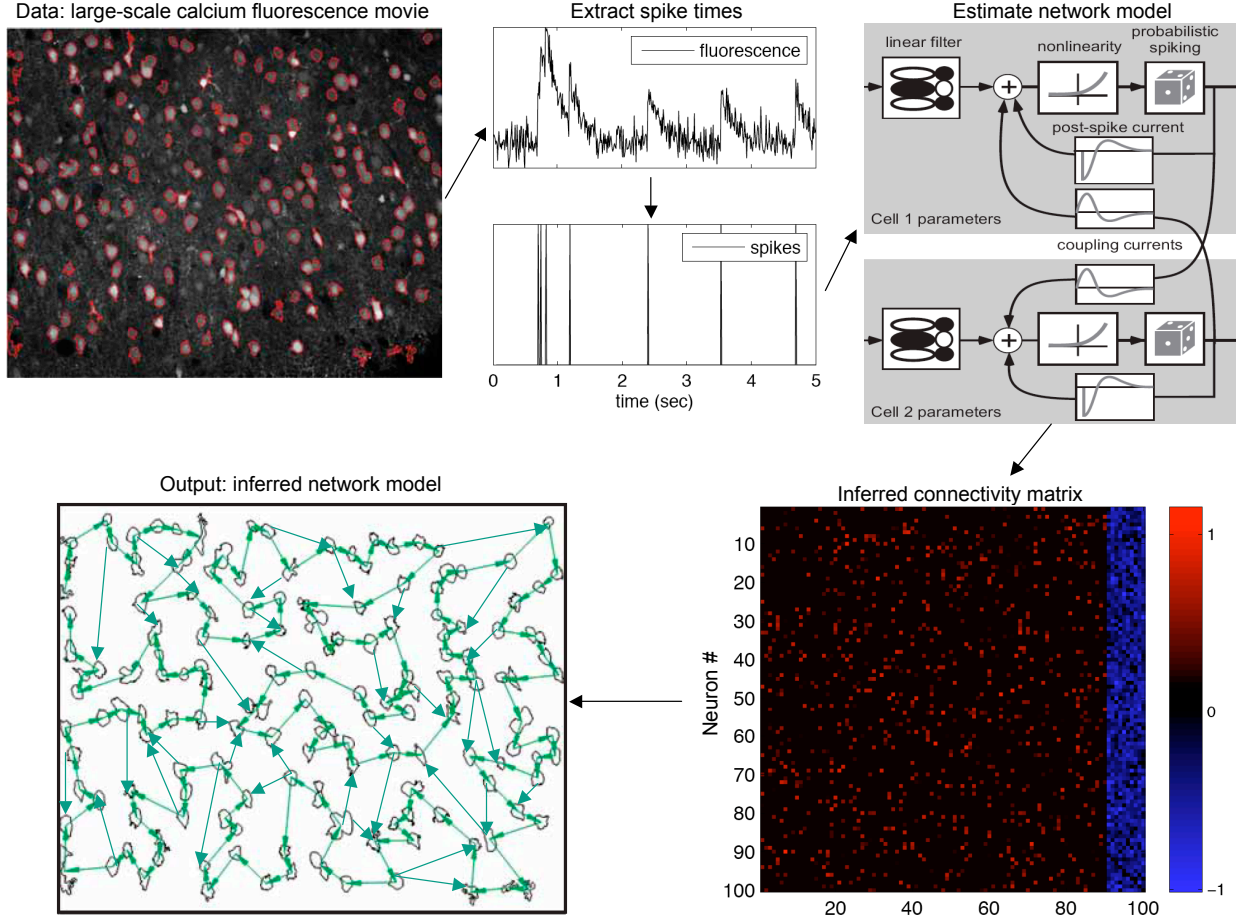


FIG. 2: Schematic overview. First we obtain large-scale calcium recordings of spontaneous and evoked neural responses. These movies are then pre-processed to correct for movement artifacts, find regions-of-interest, and extract spike trains. Second, given the fluorescence traces from each neuron, we infer spike trains. Third, we use our population model to infer the most likely functional connectivity matrix, which is our approximation of the microcircuit.

to a realistic (but relatively high quality) preparation, given 10 minutes simulation time, in a population of $N = 25$ neurons. Figure 3 depicts a couple different fluorescence traces, of varying SNR. In practice, we found that for data looking like the left panel, the factorization approach is sufficient, but for data like the right panel, too much information is lost by the factorization.

To compare the quality of our inferences using only the fluorescence traces, we also estimated the weights using the true spike trains, down-sampled to the frame rates of calcium imaging. Indeed, the quality of our estimates using the fluorescence traces are worse than those obtained from the down-sampled spike trains; $r^2 = 0.57$ using the down-sampled spike trains. Note that $r^2 \rightarrow 1$ as $T \rightarrow \infty$, when using the true (i.e., not down-sampled) spike trains, as guaranteed by our model. Indeed, when using the true spike trains, $r^2 = XXX$ for this simulation. This suggests that as imaging rates increase, we can expect a corresponding increase in accuracy of our functional connectivity weight estimates.

C. Scale bias in inferred connection weights due to coarse time discretization of calcium imaging data

That all three approaches considered in Figure 4 exhibit a significant scaling bias suggests that down-sampling spike times introduces this bias. We conjectured that this is caused by the discrepancy between $\Delta \approx 15 - 30$ msec

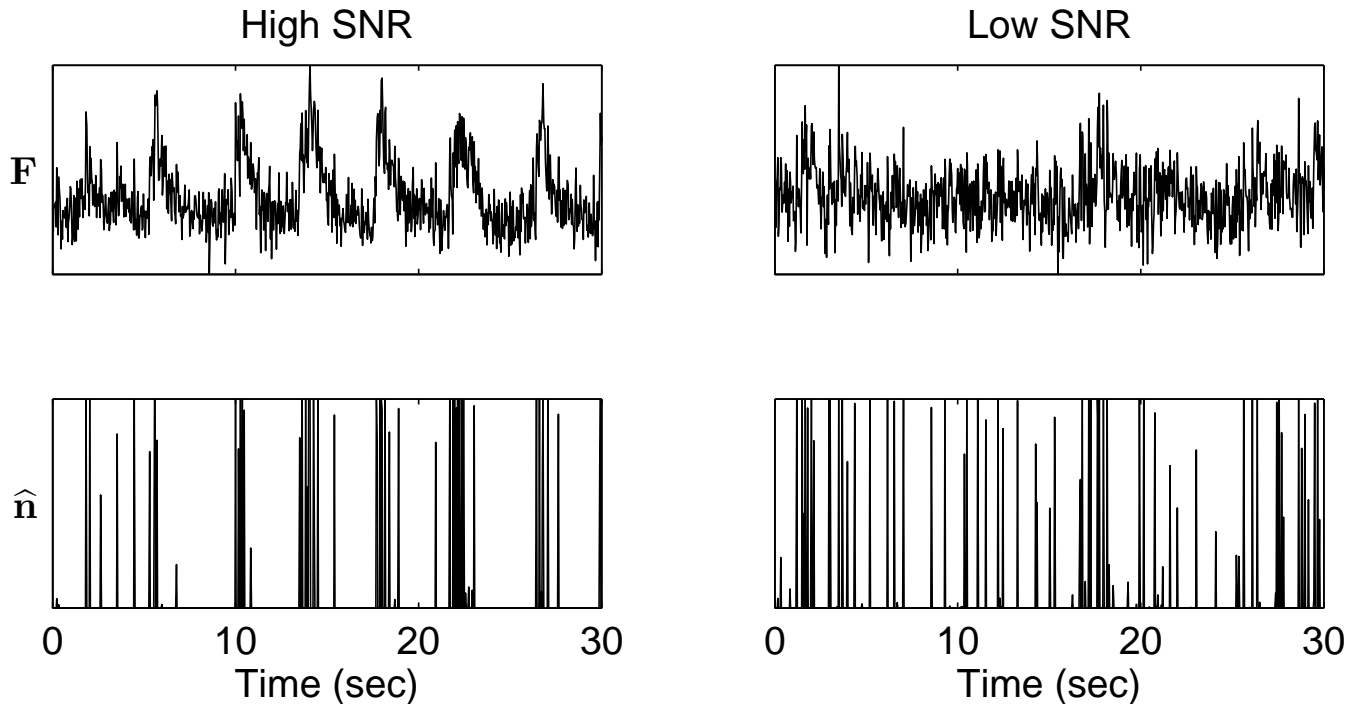


FIG. 3: Two in vivo fluorescence traces (top) and their corresponding inferred spike trains (bottom). The left panels show a high SNR case, that is sufficient quality for the factorization approximation to work nearly as well as the embedded-chain-within-Gibbs approach. The right panels show a low SNR case, in which the factorization approach is insufficient.

and the assumed PSP time scale $\approx 10 - 20$ msec. When $\Delta \gg 1$ msec, $w_{ij}h_j(t') \approx w_{ij} \exp(-\Delta/\tau_w)$, is substantially smaller than w_{ij} , and the estimated weights will be smaller than the true w_{ij} .

To estimate the magnitude of this scale bias consider two neurons coupled with weight w_{12} . Assume that, aside from this coupling, these neurons fire with baseline firing rate of $r = \exp(b)$, $b \gg w_{12}$. In order to estimate w_{12} we observe the number of spike-pairs such that the first neuron fired after the second neuron over some small period of

TABLE I: Table of simulation parameters. $\mathcal{E}(\lambda)$ indicates an exponential distribution with λ , $\mathcal{U}[a, b]$ indicates a uniform distribution between a and b , and $\mathcal{TN}[x]$ indicates a truncated normal with mean x and variance and lower bound of 30% the mean.

Total neurons	10-500
Excitatory neurons	80%
Connections sparseness	10%
Baseline firing rate	5 Hz
Mean EPSP strength	$\sim \mathcal{E}[0.5]\mu V$
Mean IPSP strength	$\sim -\mathcal{E}[2.3]\mu V$
EPSP rise time	$\sim \mathcal{U}[0.75, 1.25]$ msec
EPSP decay time	$\sim \mathcal{U}[7.5, 12.5]$ msec
IPSP rise time	$\sim \mathcal{U}[0.75, 1.25]$ msec
IPSP decay time	$\sim \mathcal{U}[15, 25]$ msec
Mean Ca noise σ_c	$\sim \mathcal{TN}[28]\mu M$
Mean Ca jump A_c	$\sim \mathcal{TN}[80]\mu M$
Mean Ca background C_b	$\sim \mathcal{TN}[24]\mu M$
Mean Ca decay time τ_c	$\sim \mathcal{TN}[0.25]$ sec
Mean photon budget α_c	1-80 Kph/neuron/frame
K_d	200 μM

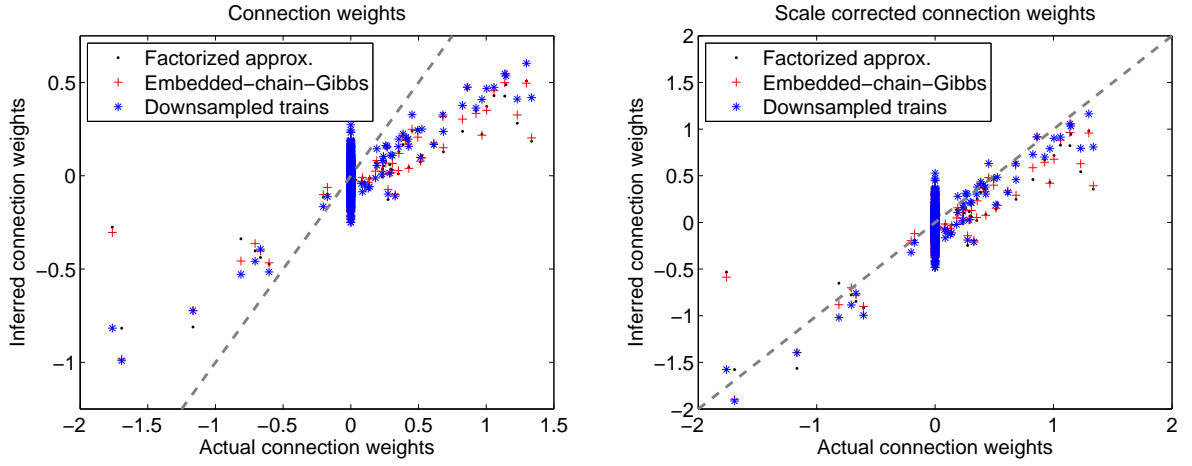


FIG. 4: Functional connectivity matrix can be reconstructed from calcium imaging data. In the upper panels inferred connection weights are shown in a scatter plot versus real connection weights, with inference performed using factorized approximation algorithm, exact embedded-chain-within-blockwise-Gibbs approach, and original spike trains observed at the frame rate of the calcium imaging. Network of $N = 25$ neurons was used, firing at ≈ 5 Hz, and imaged for $T=600$ sec at intermediate SNR (photon budget 10Kph/neuron/frame, see below). $r^2 = 0.47$ for factorized approximation algorithm was found, $r^2 = 0.48$ for embedded-chain-within-blockwise-Gibbs approach, and $r^2 = 0.57$ for the original spike trains. Thus, factorized approximation produced results almost as accurate as the exact embedded-chain-within-blockwise-Gibbs approach, and almost as accurate as the original spikes. Inferred connectivity weights (upper left) were scaled with respect to true connectivity by a constant amount due to time discretization bias (see below); other than scale, inferred connectivity represented the true connectivity matrix very well (upper right). Thus, calcium imaging is sufficient to identify connected pairs of neurons reliably.

time $\tau_w \ll T \ll 1/r$, which is in excess of the baseline firing rate $\Delta n(2 \rightarrow 1) = n(2 \rightarrow 1) - rT \approx \int w_{12} \exp(-t/\tau_w) dt$.

Now, assume that spike trains were additionally discretized into time-bins of size Δ and only the spikes that occurred in different time-bins were considered as non-coincidental. In this case, the number of spike pairs such that the spike of the first neuron followed that of the second neuron observed empirically is $\Delta n'(2 \rightarrow 1) \approx \int_0^\Delta dt_1 / \Delta \int_0^T dt_2 \exp(-(t_2 - t_1)/\tau_w)$. The ratio of the empirical count, $\Delta n'(2 \rightarrow 1)$, to that expected from GLM for given w_{12} , $\Delta n(2 \rightarrow 1)$, is the scale bias that we observe in Figure 4,

$$\Delta n'_{12} / \Delta n_{12} \approx \frac{1 - \exp(-\Delta/\tau_w)}{\Delta/\tau_w}. \quad (16)$$

In Figure 5 we plotted this estimated magnitude versus that empirically observed from our simulations for different values of Δ . As can be seen from Figure 5, simple theoretical estimate Eq. 16 describes observed scale bias quite well. In theory, this scale bias could be overcome by inferring spike trains using the superresolution sequential monte carlo algorithm from [?], which is an avenue for future exploration.

D. Impact of different imaging frame rates, durations, and noise levels on the inference

What minimal conditions for the experimental setup should be met to allow successful reconstruction of the connectivity from calcium imaging data? In Figures 6-8 we answer this question. In Figure 6, the quality of the inferred connectivity matrix is shown as function of the imaging frame rate: imaging frame rates 30-60 Hz are needed to achieve meaningful reconstruction results. These imaging frame rates are feasible for already existing experimental setups. In Figure 7 the quality of the inferred connectivity matrix is shown as function of imaging SNR, as quantified by the photon budget of the experimental setup. From our experience with the analysis of real cells [61], the photon budget in real data was ~ 10 Kph/cell/frame for in-vivo data collected at 15 Hz and ~ 100 Kph/cell/frame for in-vitro data at the same frame rate. As can be seen from Figure 7, the photon budget necessary for accurate reconstructions was 10-40 Kph/neuron/frame. For lower photon counts the amount of noise in calcium imaging data degraded inferred connectivity matrices significantly. In Figure 8 the quality of the inferred connectivity matrix is shown as function of the calcium imaging data amount from 5 min to 1 hour. The minimal necessary amount of data depended substantially on whether prior information about the distribution of connectivity weights was incorporated

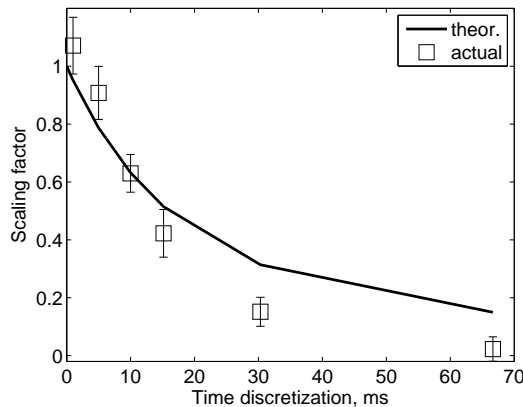


FIG. 5: Low-frame rate of calcium imaging, leading to large bin size $\Delta \approx 15 - 30$ ms of the inferred spike trains, is the reason of scale bias in the estimated connectivity matrix. This bias is explained by considering what number of causally-related spikes from a pair of neurons occur within the same time-bin for bin size Δ , and so are not considered as causally related but coincidental in the time-discretized spike trains.

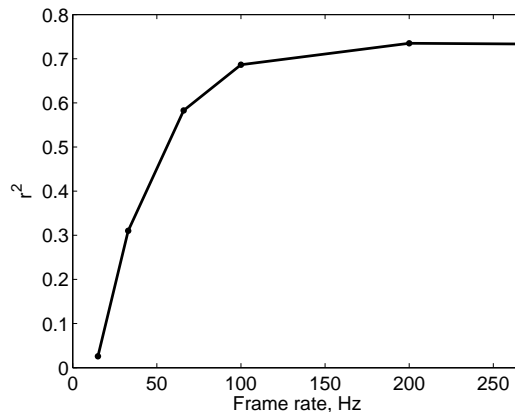


FIG. 6: Accuracy of the inferred connectivity weights as function of the frame rate of calcium imaging. Connectivity matrix here was inferred from the original spike trains observed at corresponding frame rates, thus establishing the upper performance bound for inference using calcium imaging data. A network of $N = 25$ neurons, firing at ≈ 5 Hz and imaged for $T = 600$ sec was used.

into the M-step. In particular, for M-step based on simple GLM, the calcium imaging duration necessary to achieve $r^2=0.5$ for the reconstructed connectivity matrix was $T \sim 10$ min, while for M-step solving sparse-GLM $r^2 > 0.5$ was achieved already at $T \sim 5$ min (assuming 5 Hz of firing rate). These numbers appear to be well within limitations of the existing experimental setups. Furthermore, in agreement with theoretical analysis in the Methods, the accuracy of the reconstruction did not depend on the size of imaged neural population, with the same reconstruction quality observed for the same amount of data for $N = 50 - 200$ neurons. In all cases, good reconstructions were obtained already with $T \sim 5 - 30$ min of calcium imaging data.

E. Accuracy of the estimates and Fisher information matrix

XXX THIS SHOULD PROBABLY BE REDUCED A BIT AND MOVED TO THE RESULTS; BETTER TO EXPLAIN THE RESULTS AFTER WE ACTUALLY SHOW THEM XXX

To determine the necessary amount of data for accurate estimation of the functional connectivity matrix, we calculate Fisher information for $P[\mathbf{w}|\mathbf{X}]$. Assuming for simplicity perfect knowledge of spike trains (i.e. such not corrupted by inference errors from calcium imaging) and single time-bin coupling, i.e. $h_j(t) \neq 0$ only for time-delay $t = 1$, we write the Fisher information matrix as:

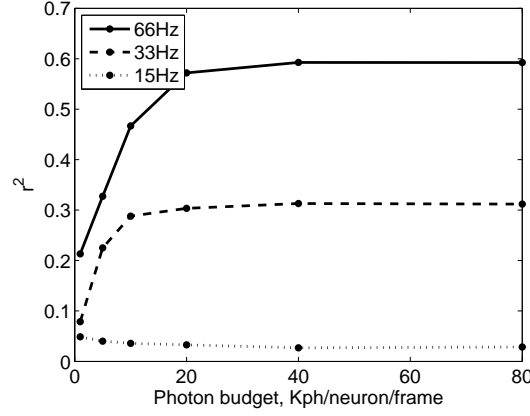


FIG. 7: Accuracy of inferred connectivity weights as function of the noise amount in the calcium imaging data, as quantified by experimental photon budget per neuron-frame, for frame rates of 15 Hz, 33 Hz and 66 Hz. Photon counts on the order of 20-40 Kph/frame/neuron are required to achieve the upper bound due by the frame rate. Connectivity matrix here was inferred from simulated fluorescence data using factorized approximation algorithm. . Simulation conditions are the same as in Figure 6.

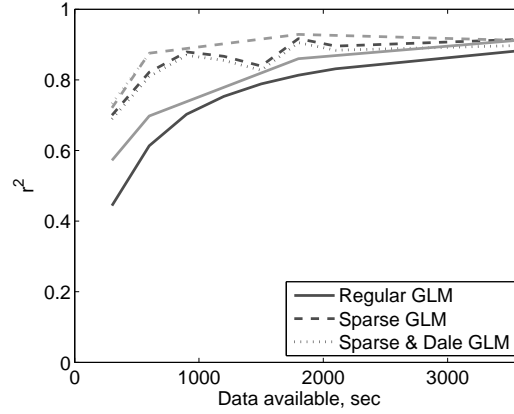


FIG. 8: Accuracy of inferred connectivity weights as function of the imaging time and neural population size. Incorporating simple priors such as exponential prior on the connectivity weights allows to boost reconstruction accuracy dramatically (dashed lines). In this latter case, $T = 300$ sec is already sufficient to recover 70% of the variance in the connection weights. Incorporating Dale's prior leads to only marginal improvement (dotted line). As shown in the methods, reconstruction accuracy does not depend on the neural population size N . Here, neural population from $N = 10$ to $N = 200$ were simulated for different T , where $N = 200$ (gray) and $N = 100$ (black) are shown. All networks were prepared in similar state by adjusting strength of inhibitory connections to achieve similar mean firing rate ≈ 5 Hz, although actual firing rate in these networks could vary. In all cases, $T = 5$ min - 0.5 hour is sufficient to produce accurate reconstructions.

$$C^{-1} = \frac{\partial(-\ln P)}{\partial w_{ij} \partial w_{i'j'}} = - \delta_{ii'} \sum_t \left[n_i(t) n_j(t-1) n_{j'}(t-1) \left(-\frac{f'(J_i(t))^2}{f(J_i(t))^2} + \frac{f''(J_i(t))}{f(J_i(t))} \right) - \Delta(1 - n_i(t)) n_j(t-1) n_{j'}(t-1) f''(J_i(t)) \right]. \quad (17)$$

where f' and f'' correspond to the first and second derivatives of our linking function (c.f Eq. 1), and $\delta_{ii'}$ is XXX ? XXX. When $f(J) = \exp(J)$ XXX Y: we don't use an exponential here. is it worth modifying this accordingly? XXX, and coupling between spikes is weak, this may be rewritten as:

$$C^{-1} = \delta_{ii'} (T\Delta) P[n_i(t) = 0, n_j(t-1) = 1, n_{j'}(t-1) = 1] E[f(J_i(t)) | n_i(t) = 0, n_j(t-1) = 1, n_{j'}(t-1) = 1] \sim (T\Delta) [(r\tau_w) \delta_{ii'} \delta_{jj'} + O((r\tau_w)^2)] r. \quad (18)$$

Here $(T\Delta)$ is the total observation time, τ_w is “the coincidence time” — the typical EPSP/IPSP time-scale over which the spike of one neuron affects the spike probability of the other neuron — and $r \approx E[f(J_i(t)) | n_i(t) =$

$0, n_j(t-1) = 1, n_{j'}(t-1) = 1]$ is the typical firing rate. For successful determination of the functional connectivity matrix \mathbf{w} , the variance C should be smaller than the typical scale $\langle \mathbf{w}^2 \rangle$, i.e.

$$(T\Delta) \sim (\mathbf{w}^2 r^2 \tau_w)^{-1}. \quad (19)$$

For typical values of $\mathbf{w}^2 \approx 0.1$, $r \approx 5$ Hz and $\tau_w \approx 10$ msec, with this order of magnitude estimate we obtain T of the order of hundred seconds. This theoretical estimate of the necessary amount of fluorescent data is in good agreement with our simulations below.

Note also that necessary recording time does not depend on the number of neurons in the imaged network N . This unexpected result is the direct consequence of the special form of C^{-1} in Eq. 18. In particular, when $r\tau_w \ll 1$, this matrix is dominated by the diagonal term $(T\Delta)(r^2\tau_w)$, and so the Fisher information matrix is predominantly diagonal with the scale $(r^2\tau_w T\Delta)^{-1}$, independent of the number of neurons N . This theoretical result is also directly confirmed in our simulations below.

F. Impact of using priors on the inference

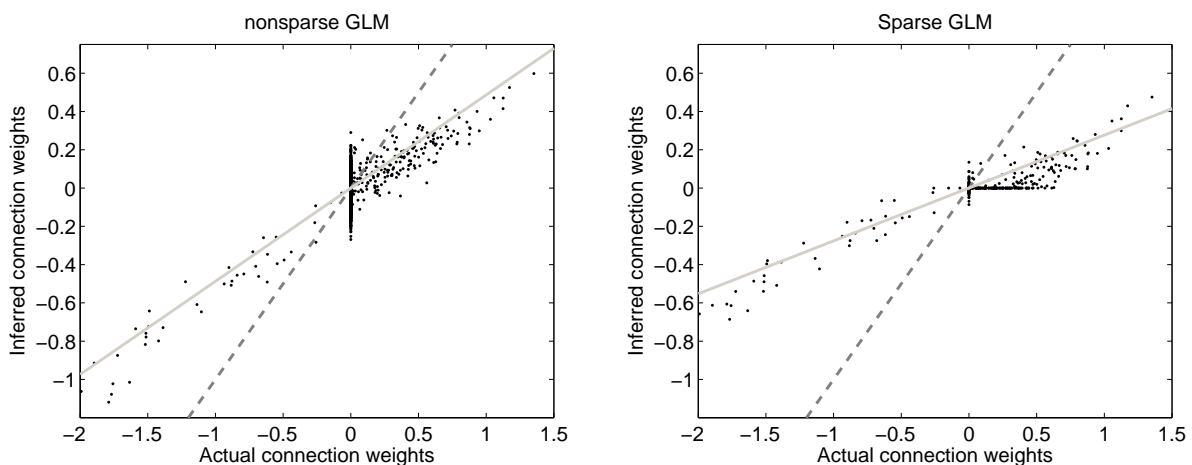


FIG. 9: Incorporating simple priors on the distribution of connectivity weights in the Bayesian inference algorithm, such as exponential sparseness prior, is essential to achieve much more accurate reconstructions than using simple GLM from a smaller amount of calcium imaging data. Here, connection weights reconstructed using simple GLM (left panel) or sparse-prior GLM (right panel) are shown in a scatter plot for a network of $N = 50$ neurons firing at ≈ 5 Hz and imaged for $T = 600$ sec. $r^2 = 0.64$ for simple GLM solution and $r^2 = 0.85$ for sparse-GLM solution.

Taking into account simple prior information about the connectivity matrix resulted in dramatic improvement of the inferred connectivity matrix, Figure 9 and 10. Sparseness prior resulted in dramatic improvements allowing successful reconstruction from as little as 5 min of calcium imaging data, and allowing to achieve for $T \approx 10$ min the same level of accuracy that would otherwise require up to $T \approx 1$ hour of calcium imaging data, Figure 8 and 9. Note, however, that sparse prior resulted in added scale bias into obtained connectivity estimate, thus, effectively destroying information about the scale of connection weights in a population. Furthermore, information about connected neural pairs and about inhibitory or excitatory nature of particular neuron could be reliably obtained, Figure 10. Dale's prior, on the other hand, only led to 10% in the correlation coefficient r^2 of the reconstructed connectivity matrix, and was not found significant.

G. Impact of strong correlations and deviations from generative model on the inference

“Anatomical” connectivity was recovered in our experiments despite potential problems noted in the literature [XXX], e.g. such as common input from correlated neurons. This is primarily due to the particular form of the activity in our neural networks, whereas firing of neurons occurred independently, thus, allowing GLM explore the full range of possible input configurations and disentangle common inputs.

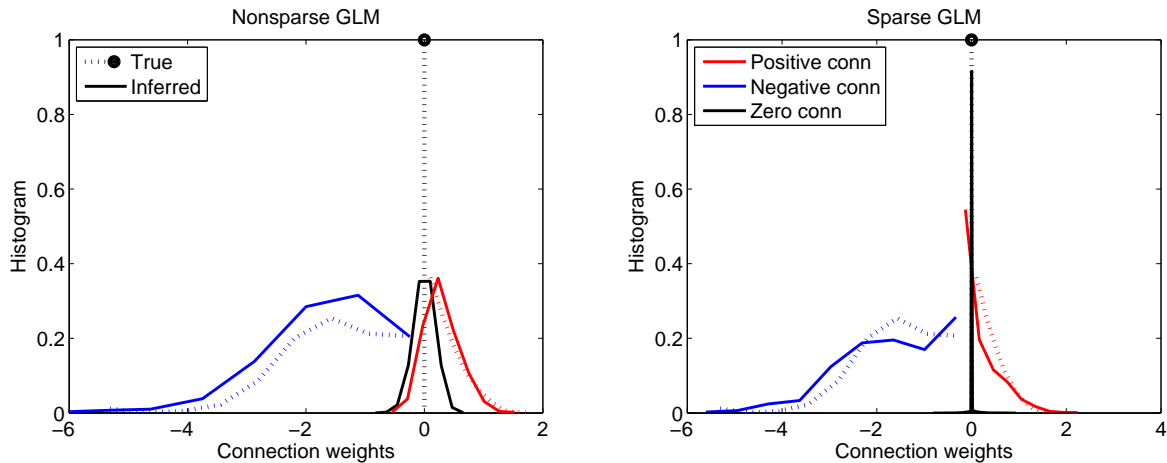


FIG. 10: Distribution of inferred connection weights using simple GLM (left) and sparse GLM (right) vs true distributions. When sparse exponential prior on the distribution of connection weights is enacted, dispersion in inferred connection weights is substantially reduced and, in particular, it becomes possible to reliably determine which neural pairs are connected. Distributions are shown for a network of $N = 200$ neurons firing at ≈ 5 Hz and imaged for $T = 600$ s was used here.

Estimation of the functional connectivity is fundamentally routed in observing changes in the spike rate conditioned on the state of the other neurons. Intuitively, such estimation can be compared to observing changes in $p(\mathbf{n}(t)) = \exp(\sum_j w_{ij} n_j(t))$ for different neural configurations $\mathbf{n}(t)$, i.e. estimating a vector \mathbf{w}_i from a number of dot-products $\mathbf{w}_i \cdot \mathbf{n}(t)$ with different vectors $\mathbf{n}(t)$. In order to properly estimate all components of \mathbf{w}_i the set of available $\mathbf{n}(t)$ should be rich enough to span all N dimensions of \mathbf{w}_i . In case of independent firing such condition is clearly satisfied. Should this condition be violated, however, e.g. due to high correlation between spiking of few neurons, spike trains may not provide access to the complete vector \mathbf{w}_i , and the connection weights inferred from such activity data may effectively “aggregate” true connection weights in arbitrary linear combinations.

We carried out a simulation of hypothetical “strongly” coupled neural network, where in addition to weak sparse connectivity we introduced sparse random strong connectivity component. In some sense, we allowed a fraction of neurons to couple strongly to the other neurons, thus making them “command” neurons “driving” activity of the other neurons. The strength of strong connectivity component was chosen to build up the actual firing rate dynamically from the baseline rate of $r = \exp(b) \approx 1$ Hz to ≈ 5 Hz. Such neural network showed patterns of activity very different from the weakly coupled networks inspected above, Figure 11. In particular, large number of highly correlated, synchronously locked firings of many neurons were evident in this network. Likewise, our algorithm was not able to identify the true connectivity matrix correctly, Figure 11.

On the other hand, our inference algorithm showed significant robustness to different deviations from the generative model. One important deviation that is likely to be present in the real data is variations in the time-scales of EPSPs of different synapses. Up to now, all EPSP time-scales τ_w were assumed to be the same in our inference algorithm. Variability in τ_w would result in added variance in the estimated weights w_{ij} through τ_w dependence of the scaling factor Eq.(16). Still, we found that such added variance to be insignificant in our simulations with τ_w varying for up to 25%, Figure 12.

IV. DISCUSSION

a. *j*'s outline of discussion

- summary of main point: using sparse prior, we can recover a large fraction of variance of connection weights, assuming reasonable SNR, parameters, and imaging rate.
- h_j vs. h_{ij} reduces dimensionality of hidden space to $O(N)$ vs. $O(N^2)$, leading to our approach scaling well as $N \rightarrow \text{big}$
- $P(A|BC) \neq P(A|B)P(A|C)$ unless B and C are uncorrelated. we use this property, correlation coefficient doesn't, cross-correlations, etc., do not.
- for the same reason, hidden neurons might be a problem for us. faster imaging, etc., should help alleviate that.

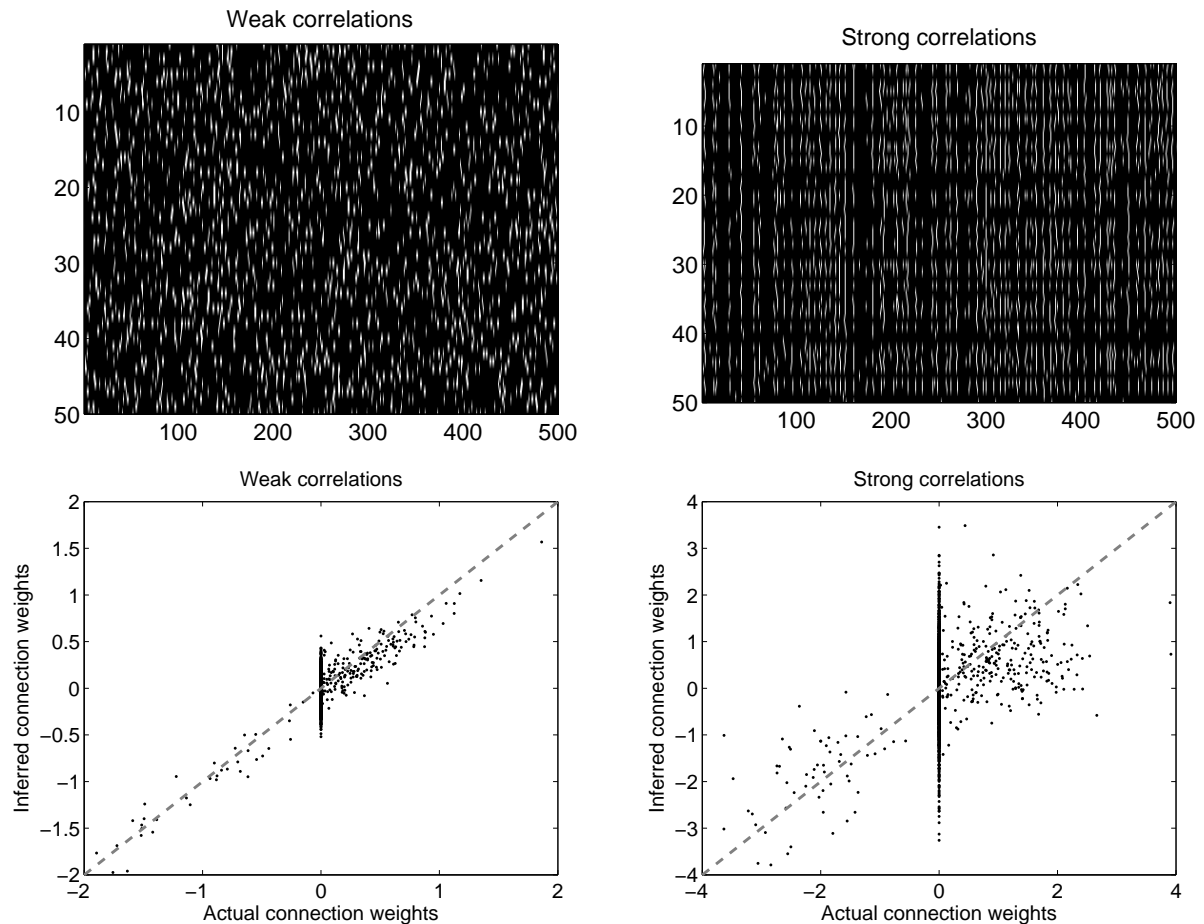


FIG. 11: Diverseness of observed neural activity patterns is required for functional connectivity to give access to the actual “anatomical” structure of the neural circuit. Here, 15 sec of simulated spike trains for a weakly coupled network (upper-left) and a network with strongly coupled component (upper-right) are shown. In weakly coupled network spikes are sufficiently uncorrelated to give access to all different neural activity patterns needed to properly estimate true weights \mathbf{w}_i . In strongly coupled case, many instances of highly synchronous locked firings are evident, thus preventing observation of sufficiently rich ensemble of activity patterns. Accordingly, GLM solution for the strongly coupled neural network (lower-right) does not represent the true connectivity of the circuit, even for the weakly coupled circuit’s component. This is contrary to the weakly-coupled network (lower-left) where true connectivity is successfully estimated. Networks of $N = 50$ neurons firing at ≈ 5 Hz and imaged for $T = 600$ sec were used to produce this figure.

- we can measure uncertainty in estimates, and use photo-stimulation to activate/deactivate small groups of neurons efficiently to help reduce variance in uncertainty.
- certainly the issue of common input and unobserved neurons should be addressed a bit more in the discussion.
- we can also talk a bit more about future directions involving fully-bayesian inference of the parameters (ie, MCMC over the parameter space, not just over the hidden variables \mathbf{X}) instead of the MAP approach we took here; i tried to set this up a bit in the methods.
- other important future work to mention: real data, faster mcmc sampling methods, dealing with nonstationarities (e.g. bleaching).
- comparison with other work (e.g., duane’s, Garofalo, Vakorina, transfer entropy, granger causality, etc.)

b. scale bias discussion Scale bias in principle may be removed by performing inference of the spike trains with the bin size $\Delta \rightarrow 0$. However, we were not successful in performing this calculation. One problem that we encountered with this approach was the increase in the variance of the connectivity estimates. In Eq.(??) the coincident time bin $t = t'$ was omitted from the sum and so all spike pairs within the same time-bins were removed from the GLM fit. Because time position of such spike pairs inferred from fluorescence data typically would have inaccuracy $\approx \Delta$,

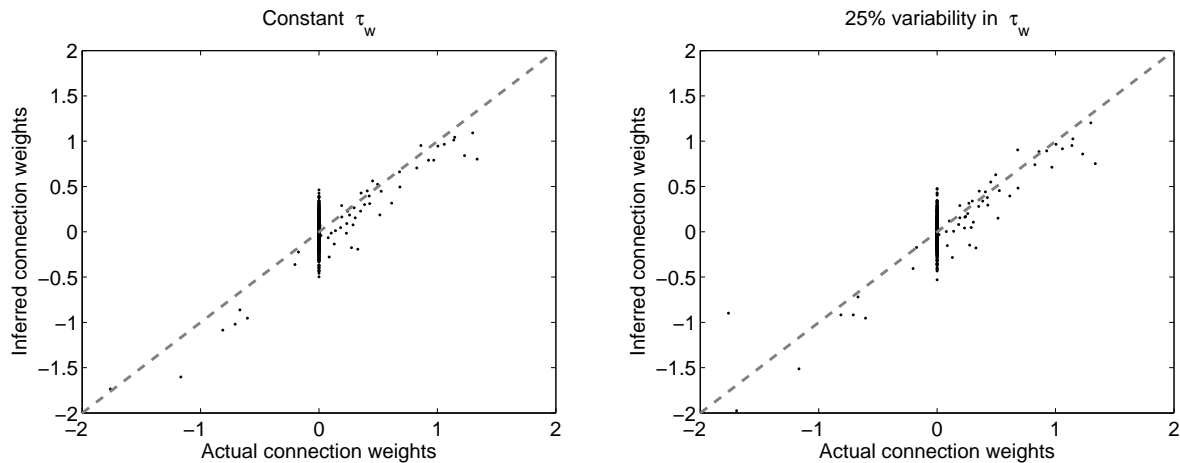


FIG. 12: Bayesian inference algorithm is robust to distortions of the underlying generative model. One distortion that should be expected is variability of the EPSP time courses from neuron to neuron, and possibly synapse to synapse. With up to 25% variability allowed in EPSP time scales τ_w (right panel) our algorithm provided reconstructions of the same quality as when all τ_w were the same (left panel). Simulation conditions are the same as in Figure 6.

temporal order of such spike pairs could often be confused, introducing ambiguity as to whether observed event should contribute to w_{ij} or w_{ji} .

Really, if the number of spikes of one neuron following that of another neuron within Δ was $n(2 \rightarrow 1)$, while such in the reverse order was $n(1 \rightarrow 2)$, difference $\delta n_{12} = n(2 \rightarrow 1) - n(1 \rightarrow 2)$ would correspond to the difference of functional connectivity weights $\delta w_{12} = w_{12} - w_{21}$. However, when such spike pairs had had their order confused with large probability $p \approx 1/2$, the number of spike pairs $n(2 \rightarrow 1)$ actually observed would become $(1 - p)n(2 \rightarrow 1) + pn(1 \rightarrow 2)$, and similarly for the reverse. Empirically observed difference $w_{12} - w_{21}$ thus would correspondingly drop to $\delta w'_{12} = (1 - 2p)\delta w_{12}$, while the variance would remain the same. This effect complicated estimating of the functional connectivity matrix W by effectively mixing w_{12} and w_{21} and introducing large error in W estimates, moving them toward $(W + W^T)/2$. We observed that the amount of data necessary to overcome this noise due to disordering of closely positioned spike-pairs appeared to be well over ≈ 10 min of data used for the most of the calculations shown in this section below. Such high-time-resolution samples of spike trains also were substantially more computationally expensive to obtain and work with. For these reasons, we did not pursue this line of research further, although it may be of interest in the future.

Acknowledgements

Thank everyone for their help and support [Bows, Bows, Bows] !!!

-
- [1] M. Abeles, *Corticonics*, Cambridge University Press, 1991.
 - [2] C. Andrieu, A. Doucet, and A. Holenstein, *Particle markov chain monte carlo*, Working paper (2007).
 - [3] Peter Bickel, Bo Li, and Thomas Bengtsson, *Sharp failure rates for the bootstrap particle filter in high dimensions*, Pushing the Limits of Contemporary Statistics: Contributions in Honor of Jayanta K. Ghosh (Bertrand Clarke and Subhashis Ghosal, eds.), IMS, 2008, pp. 318–329.
 - [4] Tom Binzegger, Rodney J. Douglas, and Kevan A. C. Martin, *A Quantitative Map of the Circuit of Cat Primary Visual Cortex*, J. Neurosci. **24** (2004), no. 39, 8441–8453.
 - [5] S. Boyd and L. Vandenberghe, *Convex optimization*, Oxford University Press, 2004.
 - [6] V. Braitenberg and A. Schuz, *Cortex: statistics and geometry of neuronal connectivity.*, Springer, Berlin, 1998.
 - [7] K. L. Briggman and W. Denk, *Towards neural circuit reconstruction with volume electron microscopy techniques.*, Current Opinions in Neurobiology **16** (2006), 562.
 - [8] D. Brillinger, *Maximum likelihood analysis of spike trains of interacting nerve cells*, Biological Cybernetics **59** (1988), 189–200.
 - [9] ———, *Nerve cell spike train data analysis: a progression of technique*, Journal of the American Statistical Association **87** (1992), 260–271.

- [10] E. Buhl, K. Halasy, and P. Somogyi, *Diverse sources of hippocampal unitary inhibitory postsynaptic potentials and the number of synaptic release sites*, Nature **368** (1994), 823–828.
- [11] E. J. Candes and J. Romberg, *Practical signal recovery from random projections.*, 2005.
- [12] E. Chornoboy, L. Schramm, and A. Karr, *Maximum likelihood identification of neural point process systems*, Biological Cybernetics **59** (1988), 265–275.
- [13] A. Dempster, N. Laird, and D. Rubin, *Maximum likelihood from incomplete data via the EM algorithm*, Journal Royal Stat. Soc., Series B **39** (1977), 1–38.
- [14] Maja Djuricic, Srdjan Antic, Wei R. Chen, and Dejan Zecevic, *Voltage imaging from dendrites of mitral cells: EPSP attenuation and spike trigger zones*, J. Neurosci. **24** (2004), no. 30, 6703–6714.
- [15] D. Donoho and M. Elad, *Optimally sparse representation in general (nonorthogonal) dictionaries via L^1 minimization*, PNAS **100** (2003), 2197–2202.
- [16] A. Doucet, N. de Freitas, and Gordon N., *Sequential monte carlo in practice*, Springer, 2001.
- [17] A. Doucet, S. Godsill, and C. Andrieu, *On sequential Monte Carlo sampling methods for Bayesian filtering*, Statistics and Computing **10** (2000), 197–208.
- [18] S. Escola and L. Paninski, *Hidden Markov models applied toward the inference of neural states and the improved estimation of linear receptive fields*, Under review, Neural Computation (2008).
- [19] D. Feldmeyer, V. Egger, J. Lubke, and B. Sakmann, *Reliable synaptic connections between pairs of excitatory layer 4 neurones within a single “barrel” of developing rat somatosensory cortex*, J Physiol **521 Pt 1** (1999), 169–90.
- [20] D. Feldmeyer and B. Sakmann, *Synaptic efficacy and reliability of excitatory connections between the principal neurones of the input (layer 4) and output layer (layer 5) of the neocortex*, J Physiol **525** (2000), 31–9.
- [21] S.J. Godsill, A. Doucet, and M. West, *Monte Carlo smoothing for non-linear time series*, Journal of the American Statistical Association **99** (2004), 156–168.
- [22] S. M. Gomez-Urquijo, C. Reblet, J. L. Bueno-Lopez, and I. Gutierrez-Ibarluzea, *Gabaergic neurons in the rabbit visual cortex: percentage, distribution and cortical projections*, Brain Res **862** (2000), 171–9.
- [23] A. Gupta, Y. Wang, and H. Markram, *Organizing principles for a diversity of gabaergic interneurons and synapses in the neocortex.*, Science **287** (2000), 273–8.
- [24] Vijay Iyer, Tycho M. Hoogland, and Peter Saggau, *Fast functional imaging of single neurons using random-access multiphoton (RAMP) microscopy*, J Neurophysiol **95** (2006), no. 1, 535–545.
- [25] J. Kulkarni and L. Paninski, *Common-input models for multiple neural spike-train data*, Network: Computation in Neural Systems **18** (2007), 375–407.
- [26] S. Lefort, C. Tómm, J.-C. Floyd Sarria, and C. C. H. Petersen, *The excitatory neuronal network of the c2 barrel column in mouse primary somatosensory cortex*, Neuron **61** (2009), 301–16.
- [27] K. Li and N. Duan, *Regression analysis under link violation*, Annals of Statistics **17** (1989), 1009–1052.
- [28] J. Livet, T. Weissman, H. Kang, R. Draft, J. Lu, R. Bennis, J. Sanes, and J. Lichtman, *Transgenic strategies for combinatorial expression of fluorescent proteins in the nervous system.*, Nature **450** (2007), 56–62.
- [29] G. McLachlan and T. Krishnan, *The em algorithm and extensions*, Wiley-Interscience, 1996.
- [30] K. Micheva and S. Smith, *Array tomography: A new tool for imaging the molecular architecture and ultrastructure of neural circuits*, Neuron **55** (2007), 25–36.
- [31] Y. Mishchenko, *Strategies for identifying exact structure of neural circuits with broad light microscopy connectivity probes*, Preprint: <http://precedings.nature.com/documents/2669/version/2> (2009).
- [32] Y. Mishchenko, J. Spacek, J. Mendenhall, D. Chklovskii, and K. M. Harris, *Reconstruction of hippocampal ca1 neuropil at nanometer resolution reveals disordered packing of processes and dependence of synaptic connectivity on local environment and dendritic caliber.*, Preprint: <http://precedings.nature.com/documents/2669/version/2> (2009).
- [33] R. Neal, *Slice sampling*, Annals of Statistics **31** (2003), 705–767.
- [34] R. Neal, M. Beal, and S. Roweis, *Inferring state sequences for non-linear systems with embedded hidden Markov models*, NIPS **16** (2003).
- [35] A. Ng, *Feature selection, L_1 vs. L_2 regularization, and rotational invariance*, ICML **21** (2004).
- [36] Q. T. Nguyen, N. Callamaras, C. Hsieh, and I. Parker, *Construction of a two-photon microscope for video-rate Ca^{2+} imaging.*, Cell Calcium **30** (2001), no. 6, 383–393.
- [37] D. Nykamp, *A mathematical framework for inferring connectivity in probabilistic neuronal networks*, Mathematical Biosciences **205** (2007), 204–251.
- [38] L. Paninski, *Maximum likelihood estimation of cascade point-process neural encoding models*, Network: Computation in Neural Systems **15** (2004), 243–262.
- [39] L. Paninski, M. Fellows, S. Shoham, N. Hatsopoulos, and J. Donoghue, *Superlinear population encoding of dynamic hand trajectory in primary motor cortex*, J. Neurosci. **24** (2004), 8551–8561.
- [40] C. C. Petersen and B. Sakmann, *The excitatory neuronal network of rat layer 4 barrel cortex*, J Neurosci **20** (2000), no. 20, 7579–86.
- [41] J. Pillow, J. Shlens, L. Paninski, A. Sher, A. Litke, E.J. Chichilnisky, and E. Simoncelli, *Spatiotemporal correlations and visual signaling in a complete neuronal population*, Nature **454** (2008), 995–999.
- [42] H. Plesser and W. Gerstner, *Noise in integrate-and-fire neurons: From stochastic input to escape rates*, Neural Computation **12** (2000), 367–384.
- [43] L. Rabiner, *A tutorial on hidden Markov models and selected applications in speech recognition*, Proceedings of the IEEE **77** (1989), 257–286.
- [44] Gaddum Duemani Reddy and Peter Saggau, *Fast three-dimensional laser scanning scheme using acousto-optic deflectors*,

- J Biomed Opt **10** (2005), no. 6, 064038.
- [45] G.D. Reddy, K. Kelleher, R. Fink, and P. Saggau, *Three-dimensional random access multiphoton microscopy for functional imaging of neuronal activity*, Nature Neuroscience **11** (2008), no. 6, 713–720.
 - [46] A. Reyes, R. Lujan, A. Rozov, N. Burnashev, P. Somogyi, and B. Sakmann, *Target-cell-specific facilitation and depression in neocortical circuits*, Nat Neurosci **1** (1998), 279–285.
 - [47] F. Rigat, M. de Gunst, and J. van Pelt, *Bayesian modelling and analysis of spatio-temporal neuronal networks*, Bayesian Analysis **1** (2006), 733–764.
 - [48] R. Salome, Y. Kremer, S. Dieudonne, J-F Leger, O Krichevsky, C Wyart, D Chatenay, and L Bourdieu, *Ultrafast random-access scanning in two-photon microscopy using acousto-optic deflectors*, Journal of Neuroscience Methods **154** (2006), no. 1-2, 161–174.
 - [49] R. J. Sayer, M. J. Friedlander, and S. J. Redman, *The time course and amplitude of epsps evoked at synapses between pairs of ca3/ca1 neurons in the hippocampal slice*, J. Neurosci. **10** (1990), 826–36.
 - [50] R. Shumway and D. Stoffer, *Time series analysis and its applications*, Springer, 2006.
 - [51] S. Song, P. J. Sjöström, M. Reigl, S. Nelson, and D. B. Chklovskii, *Highly nonrandom features of synaptic connectivity in local cortical circuits.*, PLoS Biology **3** (2005), e68.
 - [52] I. Stevenson, J. Rebesch, N. Hatsopoulos, Z. Haga, L. Miller, and K. Koerding, *Inferring network structure from spikes*, Statistical Analysis of Neural Data meeting (2008).
 - [53] I. H. Stevenson, J. M. Rebesch, N. G. Hatsopoulos, Z. Haga, L. E. Miller, and K. P. Kording, *Bayesian inference of functional connectivity and network structure from spikes*, IEEE Trans. Neural Systems and Rehab. **17** (2009), 203–13.
 - [54] Christoph Stosiek, Olga Garaschuk, Knut Holthoff, and Arthur Konnerth, *In vivo two-photon calcium imaging of neuronal networks*, Proceedings of The National Academy Of Sciences Of The United States Of America **100** (2003), no. 12, 7319–7324.
 - [55] A. Thompson, D. Girdlestone, and D. West, *Voltage-dependent currents prolong single-axon postsynaptic potentials in layer III pyramidal neurons in rat neocortical slices*, J Neurophysiol **60** (1988), 1896–1907.
 - [56] R. Tibshirani, *Regression shrinkage and selection via the lasso*, Journal of the Royal Statistical Society. Series B **58** (1996), 267–288.
 - [57] M. Tipping, *Sparse Bayesian learning and the relevance vector machine*, Journal of Machine Learning Research **1** (2001), 211–244.
 - [58] W. Truccolo, U. Eden, M. Fellows, J. Donoghue, and E. Brown, *A point process framework for relating neural spiking activity to spiking history, neural ensemble and extrinsic covariate effects*, Journal of Neurophysiology **93** (2005), 1074–1089.
 - [59] Roger Y. Tsien, *Fluorescent probes of cell signaling*, Ann. Rev. Neurosci. **12** (1989), 227–253.
 - [60] M. Vidne, J. Kulkarni, Y. Ahmadian, J. Pillow, J. Shlens, E. Chichilnisky, E. Simoncelli, and L. Paninski, *Inferring functional connectivity in an ensemble of retinal ganglion cells sharing a common input*, COSYNE (2009).
 - [61] J. T. Vogelstein, B. O. Watson, A. M. Packer, R. Yuste, B. Jedynek, and L. Paninski, *Spike inference from calcium imaging using sequential monte carlo methods*, Preprint (2009).
 - [62] D.J. Wallace, S.M. zum Alten Borgloh, S. Astori, Y. Yang, M. Bausen, S. Kügler, A.E. Palmer, R.Y. Tsien, R. Sprengel, J.N.D. Kerr, W. Denk, and M.T. Hasan, *Single-spike detection in vitro and in vivo with a genetic Ca2+ sensor*, Nature methods **5** (2008), no. 9, 797–804.
 - [63] R. Yasuda, E. A. Nimchinsky, V. Scheuss, T. A. Polgruto, T. G. Oertner, B. L. Sabatini, and K. Svoboda, *Imaging calcium concentration dynamics in small neuronal compartments*, Sci STKE **219** (2004), p15.
 - [64] R. Yuste, A. Konnerth, B.R. Masters, et al., *Imaging in Neuroscience and Development, A Laboratory Manual*, 2006.